ISSN 0022-4766, Journal of Structural Chemistry, 2020, Vol. 61, No. 10, pp. 1551-1567. © Pleiades Publishing, Ltd., 2020.
Text © The Author(s), 2020, published in Zhurnal Strukturnoi Khimii, 2020, Vol. 61, No. 10, pp. 1635-1651.

ANALYSIS OF LOCALIZED ORBITALS IN AZABORA DERIVATIVES OF [8] ANNULENE: IN THE VIEWPOINT OF AROMATICITY AND INDUCED RING CURRENTS*

M. Monajjemi[1]**

The electron density distributions among a series of [**8**] annulene (both ions and molecules) and its azabora derivatives, including its ions [$B_nN_nC_{(8-2n)}H_8$ (n = 1, 2, 3, 4)], are investigated by NBO and NMR analyses. The $(4n+2)\pi$ and $4n\pi$ systems (Hückel′s Rule) in these compounds are discussed via the localized orbital localization and electron localized function. A diatropic ring current (aromatic) and paratropic current (anti-aromatic) are distinguished. The natural hybrid orbital (NHO) direction and bond bending deviations from the line of nuclear centers are exhibited for understanding the states of π and σ orbitals. For $B_2N_2C_4H_8^{2-}$, $B_4N_4H_8^{2-}$, and $B_4N_4H_8^{2+}$ NBO calculations reveal that these structures are the dominant Lewis structures. In this work, for each NAO functions (core, valence, or Rydberg) the orbital occupancy and the orbital energies are discussed. In addition, the nucleus-independent chemical shifts and statistical nucleus independent chemical shifts confirm the amounts of aromaticity and antiaromaticity in these rings.

DOI: 10.1134/S0022476620100078

Keywords: aromaticity, LOL, ELF, annulene, induced current density, paratropic, diatropic.

INTRODUCTION

Annulene belongs to a series of conjugated monocyclic hydrocarbons with the general formula C_nH_n (n = even) or C_nH_{n+1} (n = odd), such as benzene ([**6**] annulene), cyclobutadiene ([**4**] annulene), cyclooctatetraene ([**8**] annulene), and cyclotetradecaheptaene ([**14**] annulene). Annulenes can be non-aromatic ([**10**]), anti-aromatic ([**12**]), or aromatic ([**6**] annulene). Cyclooctatetraene (COT) or [**8**] annulene, which is a poster child for non-aromatic molecules, was first synthesized by Richard Willstatter [1]. Coupling between COT^{2-} charge states and their mechanical conformations constructs a new position for COT^{2-} as an aromatic molecule, including electromechanical converter treatment. Planar conjugated COT^{2-} exhibits a powerful link between π-electrons in its molecular structure. Hückel′s $4n+2$ rule differentiates a monoaromatic ring from anti-aromatics with their magnetic properties.

Although COT that follows a non-planar conformation with alternating double and single bonds via the D_{2d} symmetry is not an aromatic molecule, the cyclooctatetraenide $C_8H_8^{2-}$ dianion is an aromatic ion with the suitable resonance

[1]Department of Chemical Engineering, Central Tehran Branch, Islamic Azad University, Tehran, Islamic Republic of Iran, University of Texas at Austin, Austin, Texas, United States of America; **Maj.monajjemi@iauctb.ac.ir. Original article submitted April 8, 2020; revised April 8, 2020; accepted April 30, 2020.

* Supplementary materials for this article are available to authorized users at doi 10.1134/S0022476620100078.

energy. This dianion is planar and octagonal in its structure and aromatic with the Hückel electron count of 10. Through the interaction between alternating bonds it has been confirmed that the structures of COT undergo a thermal shift bonding and ring inversion operations, including a planar transition state of D_{4h} [2-7]. In addition, the NMR data indicate that COT dianion (COT^{2-}) adopts a structure with the D_{8h} symmetry. Although the planar D_{4h} structure has a transition state (TS) with a barrier energy around 12 kcal/mol for the COT ring inversion [8-10], the D_{8h} bond switching TS lies a few kilocalories per mol higher. Actually, COT has three fundamental structural changes, including ring inversions, bond shifts, and valence isomerization (Scheme 1) [11-13].

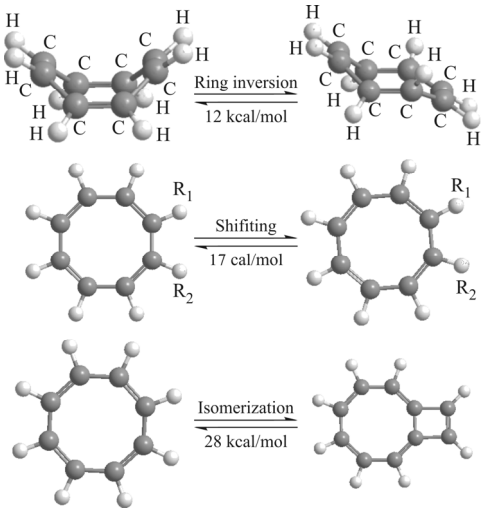

Scheme 1. Structural changes in cyclooctatetraene, including ring inversion, shifting, and valence bond isomerization.

Based on [14], studies of some ions and molecules, such as $BNC_6H_8^0$, $BNC_6H_8^{2-}$, $B_2N_2C_4H_8^0$, $B_2N_2C_4H_8^{2-}$, $B_4N_4H_8^0$, $B_4N_4H_8^{2-}$, and $B_4N_4H_8^{2+}$ help to explain the details of a theoretical link between the bond length, electron sharing, and bond energies within the context of quantum chemical topology theories. This theoretical link exhibits that structural, electronic, and energy criteria of aromaticity (ground-state aromaticity) belong to the same class and guarantees that they assess the same aromaticity property (Scheme 2).

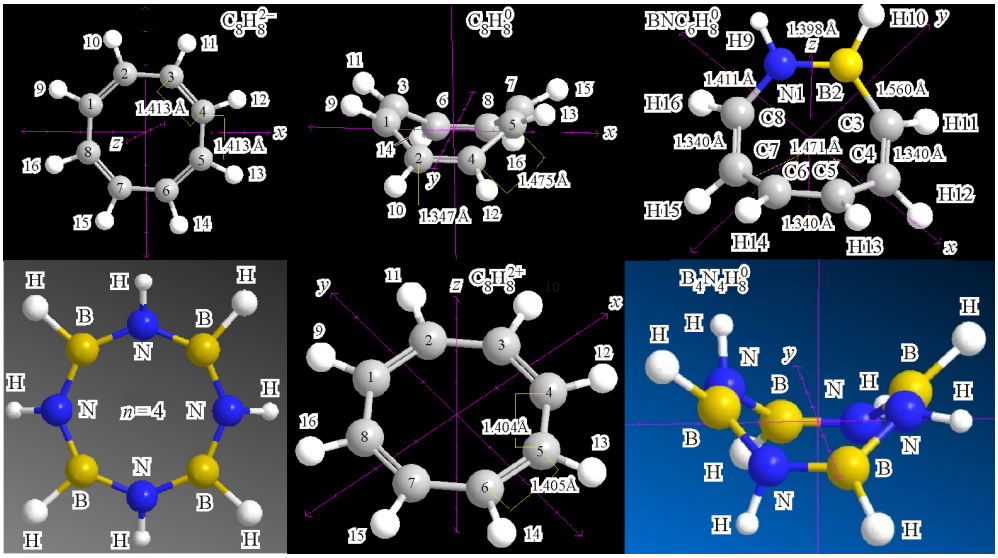

Scheme 2. Optimized geometries of $C_8H_8^{n+2}$ (n = –4, –2, 0) and $B_nN_nC_{(8-2n)}H_8$ (n = 2, 4).

Bader and Keith [15-19] investigated a model via frontier orbital contributions, which yielded an accurate result of π ring currents in benzene, COT^{2-}, and other planar rings. London [20], Pauling [21], and Pople [22] investigated the concept of aromaticity and antiaromaticity in the viewpoint of magnetic criteria, diatropic (planar $4n+2$ systems) and paratropic (planar $4n$ systems) currents. In recent decades, it has been shown that the ring current is an outcome of the HOMO–LUMO transition depending on symmetry properties and current density localized circulations around the electronegative nucleus [23]. For the $C_8H_8^{n+2}$ ($n = -4, -2, 0$) and $B_nN_nC_{(8-2n)}H_8$ ($n = 2, 4$) systems, density maps exhibit π electrons with localized circulations around the electronegative nucleus. It has been illustrated that the spread of virtual orbitals is able to compute currents in carbocyclic aromatic rings. Since $C_8H_8^{2+}$, $B_2N_2C_4H_8^{2-}$, and $B_4N_4H_8^{2-}$ have not been synthesized yet, any theoretical DFT calculation and a detailed discussion might be useful for understanding the aromaticity, physicochemical mechanism, and chemical reactions of these compounds.

RING CURRENT AND AROMATICITY

Aromaticity can be defined through magnetic criteria and is a trustworthy account of induced currents through the capabilities of external magnetic fields. In addition, chemical shift, isotropy, anisotropy, span, asymmetry, and other properties are all integrals of these current densities. Moreover, current density maps can be estimated through theoretical methods without any gauge-dependence problem. Meanwhile, from occupied to unoccupied orbitals, the total current densities are evaluated, modulated, and governed by energy divisors and symmetry rules respectively [24].

For the magnetic pattern, the outcome of all these components explains the aromaticity or antiaromaticity which is related to the net diatropicity and paratropicity of ring currents respectively. The calculation of isotropic, anisotropic parameters and chemical shift tensors σ can be performed through three independent parameters which are known as isotropic, traceless symmetric and traceless antisymmetric [25]. In addition, a spherical tensor has been exhibited by Haeberlen [26], Mehring [27], and Diehl [28]. These parameters are related to the anisotropy ($\Delta\sigma$) as $\Delta\sigma = 3/2(\delta_{zz})$ and the asymmetry (η) shielding $\eta = \left(\frac{\sigma_{yy} - \sigma_{xx}}{\sigma_{zz}} \right) = \frac{3(\sigma_{yy} - \sigma_{xx})}{2\Delta\sigma}$. The magnetic resonance of spins are seldom isotropic, therefore they must be represented by new tensors (Herzfeld–Berger notation) [29]. These tensors are known as span (Ω) $\Omega \geq 0$, which illustrates the maximum width of the model and skew (κ) of tensors which are $(\Omega) = \sigma_{33} - \sigma_{11}$ and $\kappa = \frac{3(\sigma_{iso} - \sigma_{22})}{\Omega}$. Moreover, the orientation of skew (κ) is given by $\kappa = \frac{3(\sigma_{1so} - \sigma_{22})}{\Omega}$ ($-1 \leq \kappa \leq +1$). At some points, axially symmetric tensors ($\sigma_{yy} - \sigma_{xx}$) might be zero and therefore $\eta = 0$. In addition, the asymmetry (η) indicates how a large deviation can appear from the axially symmetrical tensors, therefore the η range is $0 \leq \eta \leq +1$.

Current electron density, ELF and LOL functions. Bader [30] illustrated that regions of large electron localization have a wide range of the Fermi hole. Becke and coworkers [31] illustrated that spherically average spin-like pair had suitable correlation with the Fermi hole. Consequently, they introduced a new function as the electron localization function (ELF).

$$\mathrm{ELF}(r) = \frac{1}{1 + [D(r) / D_{0(r)}]^2}, \tag{1}$$

where $D(r) = (1/2)\sum_i \eta_i$;

$$|\nabla\varphi_i|^2 - \frac{1}{8}\left[\frac{|\nabla\rho_\alpha|^2}{\rho_\alpha(r)} + \frac{|\nabla\rho_\beta|^2}{\beta(r)} \right] \tag{2}$$

and

$$D_{0(r)} = \frac{3}{10}(6\pi^2)^{2/3}[\rho_\alpha(r)^{5/3} + \rho_\beta(r)^{5/3}] \tag{3}$$

for closed-shell systems since $\rho_\alpha(r) = \rho_\beta(r) = (1/2)\rho$. D and D_0 terms can be simplified as

$$D(r) = \frac{1}{2}\sum_i \eta_i \mid \nabla\varphi_i \mid^2 - \frac{1}{8}\left[\frac{\mid \nabla\rho \mid^2}{\rho(r)}\right] \tag{4}$$

and

$$D_{0(r)} = \frac{3}{10}(3\pi^2)^{2/3}\rho(r)^{5/3}. \tag{5}$$

Savin et al. [32] indicated which $D(r)$ determines the excess kinetic energies due to the Pauli repulsion, while $D_0(r)$ is known as the Thomas-Fermi kinetic energy term. In other words, they reconsidered ELF in the viewpoint of the kinetic energy through the Kohn-Sham DFT wave function. Therefore, ELF would be in the range [0, 1] and a large ELF value indicates that electrons are strongly localized. ELF is used for wide varieties of molecules, such as organic, inorganic, atomic crystals, coordination compounds, clusters, and also aromatic rings. Localized orbital locator (LOL) is another function similar to ELF that has been investigated by Becke and coworkers [33].

$$\mathrm{LOL}(r) = \frac{\tau(r)}{1+\tau(r)}, \qquad \text{where } (r) = \frac{D_0(r)}{\frac{1}{2}\sum_i \eta_i \mid \nabla\varphi_i \mid^2}, \tag{6}$$

$D_0(r)$ for both spin-polarized and closed-shell systems $D_0(r)$ are explained with the same meaning as in ELF.

Jacobsen exhibited that LOL supplied a more definite and obvious image than ELF, therefore LOL could be interpreted in kinetic energies better than ELF. LOL can also be interpreted in the viewpoint of localized orbitals. The LOL value ranges are similar to those of ELF: [0, 1].

NBO analysis. Electron delocalization can be defined based on Lewis data. It can be considered that the maximum electronic charges on the Lewis orbitals exhibit their low amount and correspond to strong effects of electron delocalization. In the resonance phenomenon, major and minor percentage combinations may appear in several calculations. Based on perturbation theories of the Fock matrix, it is possible to estimate donor-acceptor (bonding with anti-bonding) interactions in the NBO foundation: these analyses are carried out through examining all possible interactions among donor Lewis types (field) with acceptors (empty) non-Lewis NBOs. Their energies are calculated based on 2nd order perturbation theories. Since these interactions are related to donation of occupancies from localized to the idealized Lewis structure to empty non-Lewis orbitals, they are introduced as delocalization corrections to the zero-order natural Lewis structures. For any donor (i) and acceptor (j), the stabilization energies $E(2)$ are associated with delocalization. The equation as follows exhibits the relation of the F matrix as $E(2) = \Delta E_{ij} = q_i \frac{F_{i,j}^2}{\varepsilon_j - \varepsilon_i}$, where q_i are donor occupancies and $\varepsilon_j - \varepsilon_I$ are diagonal orbital energies. In addition, $F_{i,j}^2$ is the Fock matrix function.

COMPUTATIONAL DETAILS

Geometric and electronics structures have been calculated with advanced DFT methods using m06 and CAM-B$_3$lyp series of the functional. These methods are based on the solution of Kohn-Sham orbitals [34] and the Perdew exchange-correlation functional. The geometry of each part of ions were optimized by various methods, including M062x/cc-pvdz, M062x/cc-pvtz, CAM-B$_3$lyp/cc-pvdz, and CAM-B$_3$lyp/cc-pvtz. Ab initio calculations were accomplished for obtaining current ring data for 4n and 4n+2 carbocyclic ions ($C_8H_8^{4-}$, $C_8H_8^{2-}$, $C_8H_8^0$, and $C_8H_8^{2+}$). Induced currents were calculated

using the LEF and LOL approaches which indicate planar structures with the D_{4h} symmetry for some variants of $C_8H_8^{n+2}$ ($n = -4, -2, 0$) and $B_nN_nC_{(8-2n)}H_8$ such as $C_8H_8^{2-}$ and $C_8H_8^{2+}$ at these levels of theory. To draw the contour line maps of current densities, the Multiwfn software have been used [35, 36] for planar and fully optimized structures. The contour lines of electron densities have been plotted based on Bader′s theory [30]. These plots are needed to analyze the electrostatic surface potential distribution for each ion. Such contour lines have been plotted in gradient line maps through the same points. The relief maps were applied for presenting the height data at each center. Shaded surface maps with and without projection are applied to present the height values at each position. For confirmation the data, several extra calculations, including MP_4(SDQ)/6-31+G(*d*′), QCISD(T)/6-31+G(*d*′), and CAM-B_3lyp/6-311G have also been made. The charge transfers were also evaluated using Merz [37], chelp or chelpG [38, 39]. Those methods are based on charge fitting of electrostatic potential approaches (MESP) which are suitable for small molecules [38-45]. Electron densities, orbital values, LUMO and HOMO orbitals, electron spin densities, electrostatic charges, ELF, LOL, and total electrostatic potential (ESP) have also been calculated in this work using the multifunctional wave function analyzer [33, 34].

Among the several methods and basis sets that have been applied in this work, cc-pvdz and cc-pvtz exhibit the most desirable results for ESP fitting. In addition, polarizabilities and hyper-polarizabilities have been calculated through CISD, QCISD, and CASSCF methods. All ab initio calculations were performed using GAMESS-US and the optimization was made along with frequency calculations to confirm that the geometries were really optimal without any imaginary frequencies. This work has been accomplished based on our previous works [40-48].

RESULTS AND DISCUSSION

Although the $C_8H_8^{2+}$, $B_2N_2C_4H_8^{2-}$, $B_4N_4H_8^{2-}$, and $B_4N_4H_8^0$ compounds have not been synthesized yet, a theoretical study of these molecules and ions is essential for any further discussion and the extended theory of the induced current density. Geometric properties and optimized energies of $B_4N_4H_8^0$, $B_4N_4H_8^{2-}$, $C_8H_8^2$ obtained by various methods are listed in Table 1. It is shown that the advanced DFT methods, including m062x/cc-pvdz and m062x/cc-pvtz, yield more accurate results for negative energies, relative stabilities, C–C and C–H bond lengths, and gap energies compared to other methods, therefore, these two methods were selected to investigate and calculate other variants of these molecules (Table 1). It is now generally agreed that $C_8H_8^0$ homological rings are not aromatic, and in contrast to C_6H_6 or $C_8H_8^{2-}$, the "P" orbital electrons are localized. Using a virtual or dummy atom (Bq) in the center of rings, the nucleus-independent chemical shift (NICS) has been calculated (Table 1). NICS is a simple method developed by Schleyer and coworkers, which estimates the absolute magnetic shielding in the center of molecules. A negative NICS amount indicates aromaticity and a positive result indicates antiaromaticity. S–NICS is a statistical method computing NICSs in the viewpoint of probe motions in a sphere of shielding and deshielding spaces of molecular rings. The data on the chemical shift tensor and other NMR components are listed in Table 2. As can be seen, $C_8H_8^0$ has a both positive NICS and S–NICS, which indicates an antiaromaticity situation, while these values are negative for the other variants. The sequence of aromaticity and antiaromaticity is as follows:

A) antiaromaticity: $B_4N_4H_8^0 > C_8H_8^0 > BNC_6H_8^0 > B_2N_2C_4H_8^0$;

B) aromaticity: $B_2N_2C_4H_8^{2+} < C_8H_8^{2+} < B_2N_2C_4H_8^{2-} < B_4N_4H_8^{2-} <$ benzene $< C_8H_8^{2-}$.

Although in some cases, NICS depends on the model of basis sets (e.g., $B_4N_4H_8^{2-}$ in Table 2 and $C_8H_8^{2-}$ in Table 1), S–NICS, which is a statistical model, is independent of various basis sets. Therefore, finally for the mentioned data sequences the SNICS confirmation is needed.

The ELF current density map from ab initio calculations of $C_8H_8^{2-}$, $C_8H_8^0$, $C_8H_8^0$, $B_4N_4H_8^{2-}$, and $B_2N_2C_4H_8^0$ are shown in Fig. 1. The currents are dominated by HOMO contributions (Table 3). In a ring of the $4n+2$ system, HOMO–

TABLE 1. Geometry and Energy of $B_4N_4H_8^0$, $B_4N_4H_8^{2-}$, $C_8H_8^{2-}$ in Various Methods

Method	*X*—*X* and *X*—H (*X* = (C, B, N(T)) in ring (Å)		*X*—*X*—*X* and H—*X*—*X* angles (*X* = (C, B, N(T)) in ring	LUMO/HOMO, eV	Aromaticity	
					NICS	S–NICS
			$B_2N_2C_4H_8^0$			
CAM-B_3lyp/6-311G	*X*–*X*; B–N	1.401	NBC = 124.5	8.00	1.7	1.9
	X–*X*; C–B	1.559	CNB = 137.7			
	X–*X*; N–C	1.411	CCN = 127.2			
			$B_4N_4H_8^{2-}$			
CAM-B_3lyp/cc-pvtz	*X*–*X*; B–N	1.445	BNB = 142.6	4.50	–9.17	–8.25
	X–H; B–H	1.243	NBN = 127.4			
	X–H; N–H	1.015	HBN = 116.3			
			HNB = 108.7			
			$B_4N_4H_8^0$			
CAM-B_3lyp/cc-pvtz	B–N	1.426	HBN = 115.4	8.52	+4.19	+4.33
			HNB = 119.6			
			BNB = 140.8			
			NBN = 129.3			
			$C_8H_8^{2-}$			
MP4(SDQ)/6-31+G(*d*′)	*X*–*X*; C–C	1.415,1.100	135.0, 112.5	5.38	–14.95	–15.85
QCISD(T)/6-31+G(*d*′)	*X*–*X*; C–C	1.415,1.08	135.0, 112.5	5.38	–15.11	–15.83
CAM-B_3lyp/6-311G	*X*–*X*; C–C	1.413,1.099	135.0, 112.5	5.38	–14.87	–15.87
M062x/cc-pvdz	*X*–*X*; C–C	1.415,1.05	135.0, 112.5	5.67	–17.59	–15.88
M062x/cc-pvtz	*X*–*X*; C–C	1.409,1.094	135.0, 112.5	5.15	–15.90	–15.82

TABLE 2. Herzfeld-Berger and Haeberlen Convention of NMR Components in the M062x/cc-pvtz Calculation for $C_8H_8^0$, $C_8H_8^{2-}$, $C_8H_8^{2+}$, $B_2N_2C_4H_8^{2-}$, $B_4N_4H_8^{2-}$, and $B_4N_4H_8^0$ Compared to Benzene

Ion and molecule	σ_{11}	σ_{22}	σ_{33}	σ_{iso}	σ_{aniso} $\Delta\delta$	κ	Ω	η	NICS	S–NICS
$BNC_6H_8^0$	5.76	3.28	–18.06	–3.00	–22.5	0.79	23.8	0.16	3.00	3.11
$B_2N_2C_4H_8^{2-}$	5.52	4.13	8.93	6.19	4.1	–0.42	4.8	0.51	–6.19	–6.25
$B_2N_2C_4H_8^0$	4.21	5.08	–15.21	–1.7	–20.29	0.99	20.29	0.00	1.7	1.9
$B_2N_2C_4H_8^{2+}$	2.35	–1.53	9.89	3.56	9.48	–0.32	11.42	0.61	–3.56	–3.69
Benzene C_6H_6	5.55	6.28	13.86	8.56	7.94	–0.82	8.30	0.14	–8.56	–8.61
$C_8H_8^{2-}$	3.4	3.4	40.9	15.9	37.6	–0.99	33.7	0.0	–15.9	–15.82
$C_8H_8^0$	4.8	4.8	–21.2	–3.9	–26.0	+0.99	26	0.0	+3.9	+4.1
$C_8H_8^{2+}$	–0.17	–0.17	16,6	5.4	16.7	–0.99	16.7	0.0	–5.4	–5.5
$B_4N_4H_8^{2-\#1}$	2.55	2.55	19.14	8.08	16.59	–0.99	16.59	0.0	–8.08	–8.19
$B_4N_4H_8^{2-\#2}$	1.97	1.97	23.57	9.17	21.6	–0.99	21.6	0.0	–9.17	–8.25
$B_4N_4H_8^0$	4.96	4.98	–22.96	–4.19	–27.5	0.99	27.5	0.0	+4.19	4.33

[#1] CAM-B_3lyp/6-311G*.
[#2] CAM-B_3lyp/cc-pvdz.

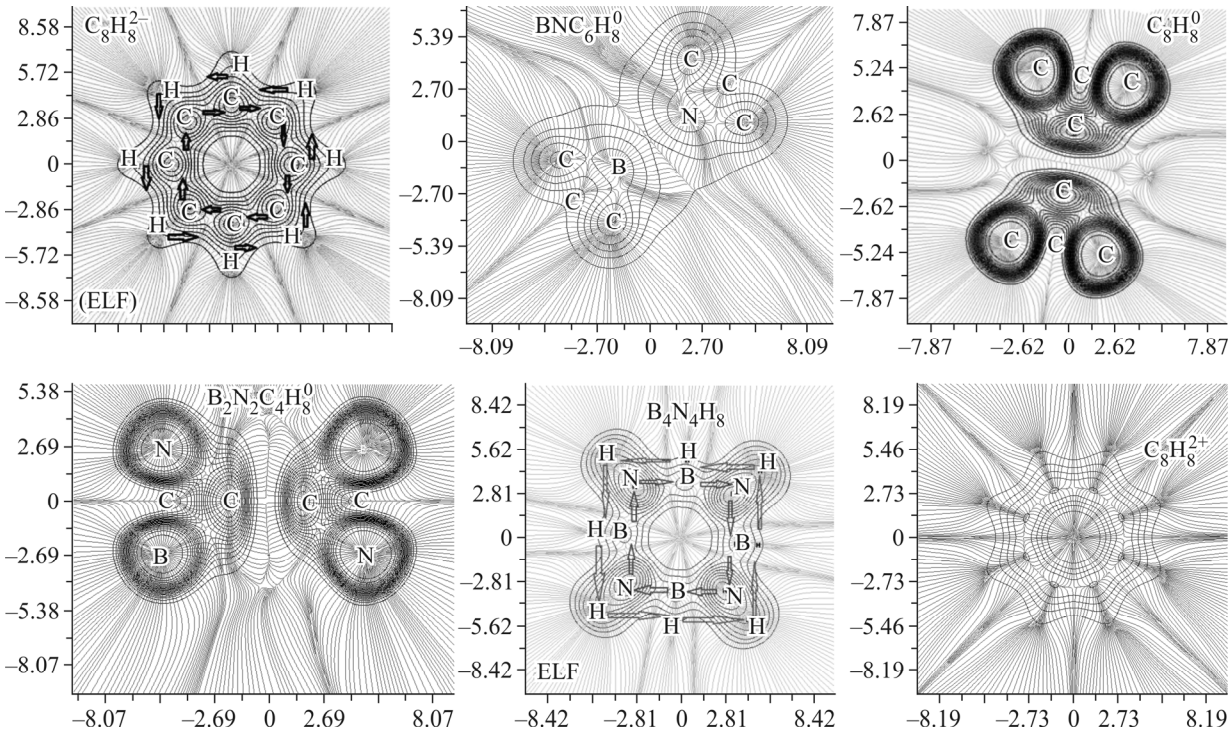

Fig. 1. Gradient line map of ELF and current density induced in cyclooctatetraene ($C_8H_8^{2-}$), ($B_4N_4H_8^{2-}$), $B_2N_2C_4H_8^0$, ($C_8H_8^{2+}$), and ($C_8H_8^0$) by a perpendicular external magnetic field calculated by the CAM-B_3lyp/cc-pvtz method. Anticlockwise circulations are diatropic, clockwise circulations are paratropic.

LUMO are related to n+1 and n, however, for a ring with 4n electrons, they are derived from split degenerate ($\lambda = n$). For $n = 4\lambda$ is zero and the diatropic contribution occurs from a transition in which $\Delta\lambda = +1$ and a paratropic contribution occurs from a transition in which $\Delta\lambda = 0$.

In Hückel′s theory for N atoms with equal Coulomb parameters $\{\alpha\}$ and equal resonance parameters $\{\beta\}$, $\{\pi\}$ energies can easily be calculated by the well-known method [48]. Therefore, for the 4n+2 systems (with higher symmetry) only the HOMO–LUMO transitions are considered (diatropic current) and for the 4n ring (lower symmetry) two forms can be considered. First, the HOMO–LUMO transition leads to a paratropic contribution, and second, HOMO–LUMO+1 transitions make diatropic contributions [49-51]. Since in the closed-shell 4n+2 systems, the occupied orbitals appear in the complete shells. The in-plane rotations of orbitals with the same $\{\lambda\}$ values can overlap, and it cannot occur from occupied-to-virtual transitions. On the other hand, the mixed adjacent orbitals must differ by $\{\Delta\lambda = \pm 1\}$. The only occupied-virtual-translational (OVT) transition in the (4n+2) system is, therefore, from HOMO to LUMO, and hence, in this monoring system, the ring current occurs only from the HOMO orbitals which are fully diamagnetic, but at $n = 0$ the HOMO has degeneracy of 2 and the (4n+2) system has four electrons in the diamagnetic situation. At 4n, the $\{\pi\}$ systems have half-filled angular moment, therefore in the full $\boldsymbol{D}_{nh}$ symmetry, it goes towards an open-shell configuration with distorted degeneracy. With reducing symmetry, HOMO and LUMO pairs split into non-degenerate orbitals related by a rotational transition with low energies. As can be seen from Table 3, gap energies (*a*), HOMO/LUMO overlap amounts (*b*), and HOMO/HOMO–1 overlap amounts (*c*) in whole spaces obey the sequence as follows: *a*, *b*, *c*. It has been shown that aromaticity sequence is a part of (*b*) and the antiaromaticity sequence is a part of (*c*), while induced current densities have a straight relation with gap energies.

(*a*): $B_4N_4H_8^{2-} < B_2N_2C_4H_8^{2-} < C_8H_8^{2-} < C_8H_8^{2+} < C_8H_8^0 < B_2N_2C_4H_8^0 < BNC_6H_8^0 < B_4N_4H_8^0$

(*b*): $B_2N_2C_4H_8^{2-} < B_4N_4H_8^{2-} < C_8H_8^{2-} < B_4N_4H_8^0 < B_2N_2C_4H_8^0 < C_8H_8^0 < C_8H_8^{2+}$

(*c*): $B_4N_4H_8^{2-} < B_2N_2C_4H_8^{2-} < C_8H_8^{2+} < B_4N_4H_8^0 < B_2N_2C_4H_8^0 < C_8H_8^{2-} < C_8H_8^0$.

TABLE 3. HOMO and LUMO Characteristics in Several Molecules from Annulene to Ion Heterocycles Based on SCPA Partition (Stout-Politzer) [52] Obtained by M062x/cc-pvTz Methods

Ion and Molecule	HOMO/LUMO Gap energy, eV	% composition of atoms for HOMO	% composition of atoms for LUMO	HOMO/LUMO overlap in the whole space	HOMO/HOMO–1 overlap in the whole space
$BNC_6H_8^0$	7.58	14.7(C3+C6)+3.05N1+ +18.89B2+13.68(C4+C5)+ +8.35C7+10.33C8	13.97(C3+C7+C8)+12.44N1+ +2.24B2+8.35C7+9.47C4+ +15.44(C5+C6)	0.754	0.846
$B_2N_2C_4H_8^0$	8.01	8.3(C1+C3)+2.6(B2+B6)+ +17.6(N4+N8)+19.2(C5+C7) The coefficients of all hydrogen atoms are zero	18.0 (C1+C3)+19.5(B2+B6)+ +4.0(N4+N8)+7.1(C5+C7)	0.658	0.723
$B_2N_2C_4H_8^{2-}$	4.055	30.0(B1+B7)+4.0(C3+C5)+ +15.9(C4+C6) The coefficients of all hydrogen atoms are zero	9.0(B1+B7)+19.4(N2+N8)– –4.7(C3+C5)+34.6(C4+C6)+9.1B7– –3.4(H9+H15)–10.0(H10+H16)+ +6.1(H11+H13)–1.1(H12+H14)	0.333	0,554
$B_4N_4H_8^{2-}$	3.54	25.0(B1+B4+B6+B7) The coefficients of all hydrogen atoms are zero	6.8(B1+B4+B6+B7)+ +11.5(N2+N3+N5+N8)– –2.6(H9+H12+H14+H15)– –9.4(H10+H11+H13+H16)	0.348	0.338
$B_4N_4H_8^0$	8.527	24.9(B2+B3+B5+B8) The coefficients of all hydrogen atoms are zero	24.8(N1+N4+N6+N7)	0.381	0.718
$C_8H_8^{2-}$	5.38	7.0(C1+C3+C5+C7)+ +17.9(C2+C4+C6+C8) The coefficient of all hydrogens are zero	14.9(C1+C3+C5+C7)+ +16.7(C2+C4+C6+C8)– –3.47(H9+H11+H13+H15)– –3.15(H10+H12+H14+H16)	0.377	0.762
$C_8H_8^0$	7.26	12.21(C1+C4+C6+C7)+ +12.01(C2+C3+C5+C8) The coefficients of all hydrogen atoms are zero	11.5(C1+C4+C6+C7)+ +13.1(C2+C3+C5+C8)	0.791	0.857
$C_8H_8^{2+}$	7.25	27.2(C1+C5)+0.0(C3+C7)+ +11.5(C2+C4+C6+C8) The coefficients of all hydrogen atoms are zero	12.5(C1+C2+C3+C4+ +C5C6+C7+C8) and the coefficients of all hydrogen atoms are zero	0.839	0.587

This means that HOMO/LUMO overlap amounts in whole spaces can be considered as an index for aromaticity while HOMO/HOMO–1 overlap is an index of antiaromaticity.

Thus, HOMO/LUMO overlapping indicate the sum over states, producing a strong two-electron paramagnetic ring current which is maximum for $C_8H_8^{2-}$ and minimum for $B_2N_2C_4H_8^{2-}$. Other rotational and translational transitions presented through the symmetry lowering are actually not important in small cycles. The $C_8H_8^{2-}$ and $C_8H_8^{2+}$ ions are structured with σ/σ^* orbitals around π/π^* molecular orbitals where the overlap of σ/π separation has been missed. On the other hand, in the systems such as $B_2N_2C_4H_8^{2-}$ and $B_4N_4H_8^{2-}$, the localization of heterocycle orbitals at a high electronegativity normally lead to loss of the ring current (Fig. 1).

In Table 4, the ring perimeter sequences for the two series are as follows:

A): $C_8H_8^{2+} < C_8H_8^0 < C_8H_8^{2-}$,

B): $B_4N_4H_8^0 < B_2N_2C_4H_8^{2-} < B_4N_4H_8^{2-}$.

TABLE 4. Ring Perimeter, Para-Delocalization (PDI), and Paralinear Response Indices (PLR) for $C_8H_8^0$, $C_8H_8^{2-}$, $C_8H_8^{2+}$, $B_2N_2C_4H_8^{2-}$, $B_2N_2C_4H_8^0$, and $B_4N_4H_8^{2-}$

Molecule	Ring perimeter, Å	PDI index	PLR index
$C_8H_8^{2-}$	11.30	0.030	0.13
$C_8H_8^0$	11.24	0.032	0.086
$C_8H_8^{2+}$	11.23	0.004	0.006
$B_4N_4H_8^{2-}$	11.56	0.031	0.16
$B_4N_4H_8^0$	11.41	0.01	0.03
$B_2N_2C_4H_8^{2-}$	11.48	0.031	0.14
$B_2N_2C_4H_8^0$	11.42	0.0279	0.064

Both A and B sequences depend firstly on the number of π electrons and secondly on the number of π orbitals. Therefore for these $B_2N_2C_4H_8^{2-}$ and $B_4N_4H_8^{2-}$ ions, it is needed to rearrange the Coulomb and resonance integral equations as: (1) boron and nitrogen atoms are zero- and two-electron donors with equal orbital energies (α–β and α+1.5β). In the structure of these molecules with different electronegativities of boron and nitrogen atoms, a symmetric change to the Coulomb parameters yields (α–γβ) and (α+γβ) energies where γ is a correlated parameter in various structures and varies in the range $0 \le \gamma < 1$. A solution of the Hückel equation via considering the γ parameter with a simple modification gives molecular orbitals {∅} and related energies {ε} from which the consequences for cycle currents can be deduced. Canonical molecular orbitals ($\Psi_{\lambda,c}$) are a delocalized set with $\gamma = 0$, and in each $\gamma \neq 0$ position, a linear combination of these set can be written for the orbitals. In the full symmetrical systems of carbocycles, the degeneracy of $\Psi_{2,c}$ and $\Psi_{2,s}$ can be stabilized in several ways, such as a distortion to D_{2d} and D_{4h} geometries of "clamped"-replaced COT systems [49-51].

Due to its bond alternation, D_{4h} COT keeps delocalized orbitals and also the cycle current of the equilateral carbocycle (Fig. 1). In the heterocyclic systems ($\gamma \neq 0$), $\Psi_{2,c}$ and $\Psi_{2,s}$ are bonding and anti-bonding wave functions which belong to B_{1u} and B_{2u} symmetries on D_{4h} subunits of the D_{8h} character. It is notable that $\Psi_{2,c}$ and $\Psi_{2,s}$ wave functions are HOMO and LUMO for all γ values, which are completely localized: HOMO on the nitrogen atom and LUMO on the boron atom. Obviously, $\varnothing_{0,c}$, $\varnothing_{1,c}$, $\varnothing_{1,s}$, $\varnothing_{3,c}$, $\varnothing_{3,s}$ and $\varnothing_{4,c}$ become strongly localized on the electronegative atoms. At $\gamma = 1$ the nitrogen and boron atoms obey Hückel′s population as $1 \pm \frac{1}{2}\left(\frac{1}{2} + \frac{1}{\sqrt{3}} + \frac{1}{2\sqrt{5}}\right) \approx 1.66$ and 0.36 electrons, respectively. In the Hückel–London approach the ring current of the eight-membered ring at small γ, the HOMO–LUMO contribution overcomes the bond–bond polarizability. With increasing γ from planar-constrained COT (where $\gamma = 0$) to planar $B_4N_4H_8$ (where $\gamma = 1$), the eight-membered ring still has a net paratropic circulation. The symmetry conclusion to deduct the line currents at the $4n\pi$ position includes several steps. Firstly ($\gamma \approx 0$), these currents are overmatched via the HOMO–LUMO transitions amongst small gap energies. This situation ($\Delta\lambda = 0$) generates large paratropic intensities. In other words, the symmetry reasoning for deducing currents in $4n$ systems consists of several levels from $\gamma = 0$, when the current is induced by the HOMO–LUMO transition with a small energy gap, to $\gamma = 1$,when the HOMO–LUMO gap opens, and the intensities of the currents fall but remain paramagnetic. Here the HOMO–1 and LUMO separation as well as HOMO and LUMO+1 increases slowly, and the paratropic or anti-aromatic cycle current is reduced significantly (Tables 2 and 3). Investigation of the symmetry can be applied for understanding ring and perimeter currents in these systems. Ring perimeters (Å) and areas (Å^2) of these molecules are listed in Table 3. Based on these data, the ring perimeters and areas have a nonlinear relationship due to the non-geometrical behavior of aromaticity in heteromolecules, including boron and nitrogen atoms.

As can be seen from Table 4, the ring perimeters (Å) for three levels of molecules (*a*, *b*, and *c*) obey the sequences as follows. Both sequences of *b* and *c* ring perimeters are in contrast to the HOMO/HOMO–1 overlap while the a sequence is in contrast to the HOMO/LUMO overlap: (*a*) $C_8H_8^{2+} < C_8H_8^0 < C_8H_8^{2-}$; (*b*) $N_4B_4H_8^0 < N_4B_4H_8^{2-}$; (*c*) $N_2B_2C_4H_8^0 < N_2B_2C_4H_8^{2-}$.

In Table 4, the aromatic fluctuation index is close to zero, the delocalization indices are acceptable for these systems, and the PLR indices for aromaticity are larger than those for antiaromaticity. As can be seen in Table 3, the HOMO coefficient of all hydrogen atoms is zero or close to zero (in the% atomic composition for HOMOs), and also in some molecules, these coefficients for some atoms in the rings are zero, e.g. (C3+C7). In contrast to LUMO, the hydrogen atom plays a considerable role in the percentage of composition, therefore the gap energies are related to the number of hydrogen atoms, which are equal for all variants. This means that HOMO, LUMO, and gap energies depend only on the rings in the viewpoints of aromaticity, antiaromaticity, and induced currents.

Based on the NBO analysis (Tables 5-7) and Fig. 2, the natural hybrid orbital (NHO) directions and bond bendings (deviations from the line of nuclear centers) can be estimated for understanding the state of π and σ orbitals. These data are often useful for the predication of the geometry direction changing the results of geometry optimizations. The direction of a hybrid is specified in terms of the polar (θ) and azimuthal (φ) angles of its vector describing *p*-component. The hybrid

TABLE 5. NHO directions And Bond Bending Deviations from the Line of Nuclear Centers in Variants of $[B_nN_nC_{(8-2n)}H_8$ (n = 2, 4)]

NBO	Line of centers		Hybrid 1			Hybrid 2			Wave function	OCC
	θ	φ	θ	φ	Dev	φ	θ	Dev		
						$B_4N_4H_8^{2-}$				
B1–N2 (σ)	90.0	107.6	90.0	104.5	3.1	90.0	290.4	2.8	$0.47SP^{2.06}$ of B1 + 0.88 $SP^{1.37}$of N2	1.98
B1–N3 (π)	90.0	340.2	0.0	0.0	90.0	0.0	0.0	90.0	0.45 P^1 of B1 + 0.89 P^1 of N3	1.98
N2–B4 (π)	90.0	70.2	0.0	0.0	90.0	0.0	0.0	90.0	0.45 P^1 of B4 + 0.89 P^1 of N2	1.98
N2–B4 (σ)	90.0	70.2	90.0	67.4	2.8	90.0	253.3	3.1	$0.47SP^{2.06}$ of B4 + 0.88 $SP^{1.37}$of N2	1.88
N3–B6 (σ)	90.0	17.6	90.0	20.4	2.8	90.0	194.5	3.1	$0.47SP^{2.06}$ of B6 + 0.88 $SP^{1.37}$of N3	1.98
N5–B7 (π)	90.0	340.2	0.0	0.0	90.0	0.0	0.0	90.0	0.45 P^1 of B7 + 0.89 P^1 of N5	1.88
						$B_4N_4H_8^0$				
N1–B2 (σ)	90.1	69.0	90.0	65.7	3.3	89.9	252.5	3.6	$0.47SP^{2.06}$ of B1 + 0.88 $SP^{1.46}$of N2	1.98
N1–B2 (π)	90.1	69.0	0.1	352.6	90.1	179.9	230.3	90.0	0.31 P^1 of B4 + 0.94 P^1 of N2	1.88
N1–B2 (π*)	90.1	69.0	0.1	352.6	90.1	179.9	230.3	90.0	0.31 P^1 of N1* + 0.94 P^1 of B2*	0.166
B2–N4 (σ)	90.1	18.2	90.1	14.7	3.6	90.0	201.5	3.3	$0.47SP^{2.06}$ of B2 + 0.88 $SP^{1.46}$of N4	1.98
N6–B3 (π)	90.1	333.9	0.1	308.5	90.0	0.1	242.2	89.9	0.31 P^1 of B3 + 0.94 P^1 of N6	1.83

TABLE 6. Occupancy Threshold for a Suitable Pair, Total Populations of Lewis and Non-Lewis Orbitals, the Number of Core (CR), 2-Center Bond (BD), Lone Pair (LP) NBOs in the Natural Lewis Structure, the Number of Low-Occupancy Lewis (L) and High-Occupancy (> 0.1 e) Non-Lewis (NL) Orbitals, and the Maximum Deviation (Dev) of any Formal Bond Order for the Structure From a Nominal Estimate (NAO Wiberg Bond Index) for Several Compounds

Compound	Threshold	Lewis	Non-Lewis	CR	BD	LP	L	NL	Dev
$B_2N_2C_4H_8^0$	1.90	55.37163	0.62837	8	20	0	0	1	0.04
$B_4N_4H_8^0$	1.90	54.36132	1.63868	8	16	4	4	4	0.03
$B_4N_4H_8^{2-}$	1.90	55.04936	2.95064	8	16	5	5	3	0.17
$C_8H_8^0$	1.90	55.30840	0.69160	8	20	0	0	0	0.05
$C_8H_8^{2-}$	1.90	53.81485	4.18515	8	16	5	5	3	0.36

TABLE 7. Donors and Acceptors of Some Bonds in $B_4N_4H_8^0$

Donor NBO (*i*)	Acceptor NBO (*j*)	*E*(2), kcal/mol	*E*(*j*) – *E*(*i*), a.u.	F(*i*,*j*), a.u.
		$B_4N_4H_8^0$		
N1–B2 (σ)	(N1–H9)*	2.03	1.28	0.45
N1–B2 (π)	RY*B3	1.18	1.49	0.039
N1–B2 (π)	(B3–N6)*	50.21	0.43	0.132
N1–B2 (π)	(N1–B2)*	1.38	0.43	0.022

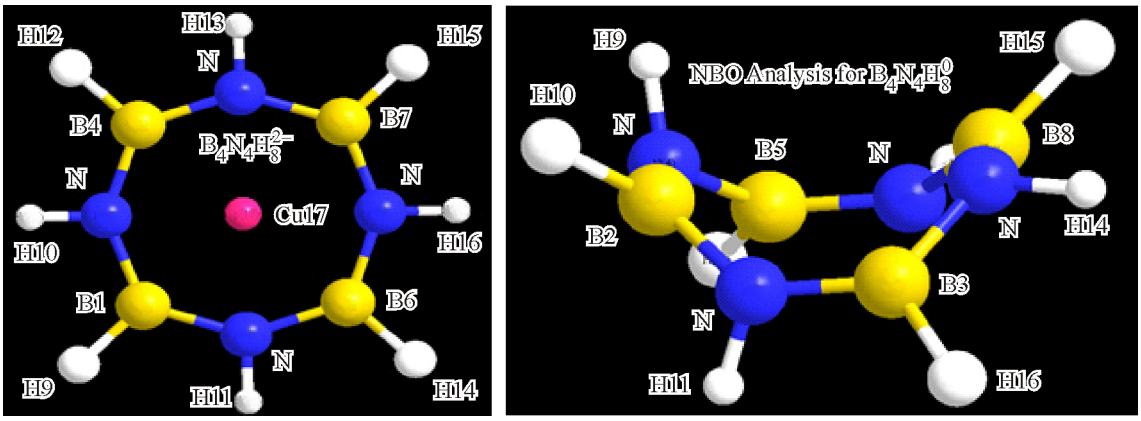

Fig. 2. Optimized structures of $B_4N_4H_8^{2-}$ and $B_4N_4H_8^0$ with atomic numbering.

directions are then compared with the directions of lines of the centers between two nuclei for determining the bending of these bonds, which is expressed as deviation angles between these two directions. For $C_8H_8^{2-}$, $B_4N_4H_8^0$, and $C_8H_8^{2+}$ the NBO calculations exhibit that these structures are mainly Lewis ones. However, based on the advanced valence bond theory, covalent-ionic resonances are not necessary due to the inclusion of bond polarity effects in a resonance structure. In this work, the orbital occupancy and the orbital energy are shown for each NAO function (core, valence, or Rydberg) and it is notable that the occupancies of Rydberg (Ryd) NAOs are typically much lower than those of the core and valence (Val) NAOs of the natural minimum basis (NMB) set.

In addition, the occupancy threshold for the estimation of total populations of Lewis and non-Lewis NBOs, the number of core (CR), 2-center bond (BD), 3-center bond (3C), and lone pair (LP) NBOs in the natural Lewis structure, the number of low-occupancy Lewis (L) and high-occupancy non-Lewis (NL) orbitals, and the maximum deviation (Dev) of any formal bond order for the structure from a nominal estimate have been considered for $C_8H_8^{2-}$, $C_8H_8^{2+}$, $B_2N_2C_4H_8^0$, $B_2N_2C_4H_8^{2-}$, and $B_4N_4H_8^{2-}$ (Supplementary Materials). For instance, in $B_4N_4H_8^{-2}$ (Table 5) nitrogen NHOs of the B1–N2 (σ) bond is bent away from the line of B–N centers by 3.1° for Hybrid 1 and 2.8 for Hybrid 2. The N–H bonds of B1–N3 (π) is bent by even 90.0, which indicates pure π. The information in these tables is a summary of all calculations, therefore for any further information the output NBO, NMR, and optimization files of the variants are given in the Supplementary Materials.

For instance (Table 7), the N_1–B_2 (π) (B3–N6)* interaction between the N_1–B_2 bond and the planar B3–N6* anti-bond is seen to give a strong stabilization of 50.21 kcal/mol with the F matrix of 0.132. For any further information, please, refer to the Supplementary Materials.

A symmetrical electron density distribution and LOL densities, including DOS, PDOS, TDOS, and OPDOS for $B_4N_4H_8^{2-}$, can be seen in Fig. 3, which indicates that these two compounds are isostructural to each other and $C_8H_8^{2-}$ (Fig. 4). Although the density of states for a single molecule has no physical meaning, to get some information about

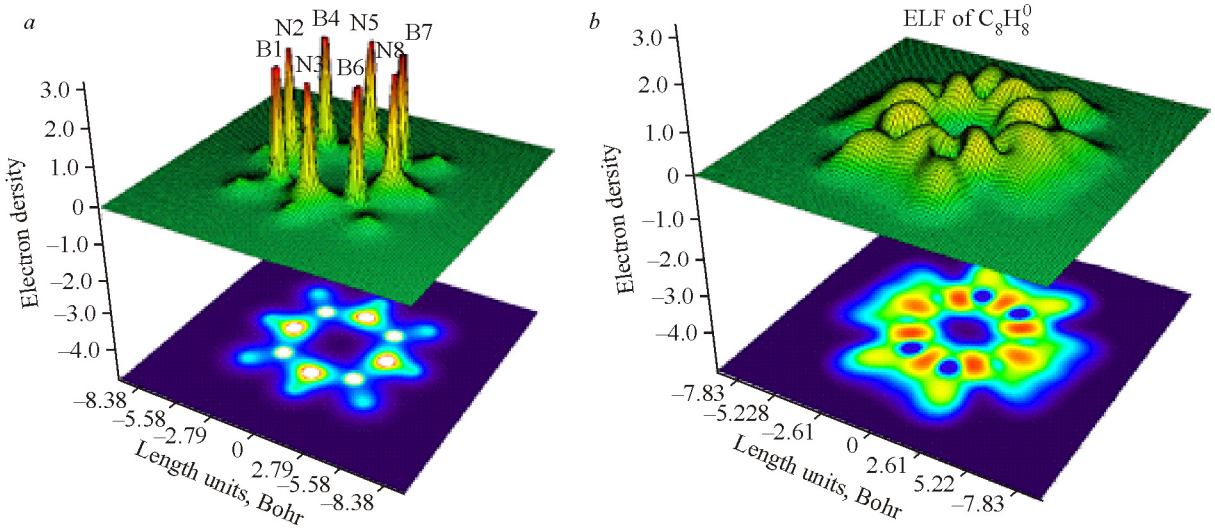

Fig. 3. Shaded surface map with the projection of the density of states: ELF total electron density (*a*) and LOL density of $C_8H_8^0$ (*b*).

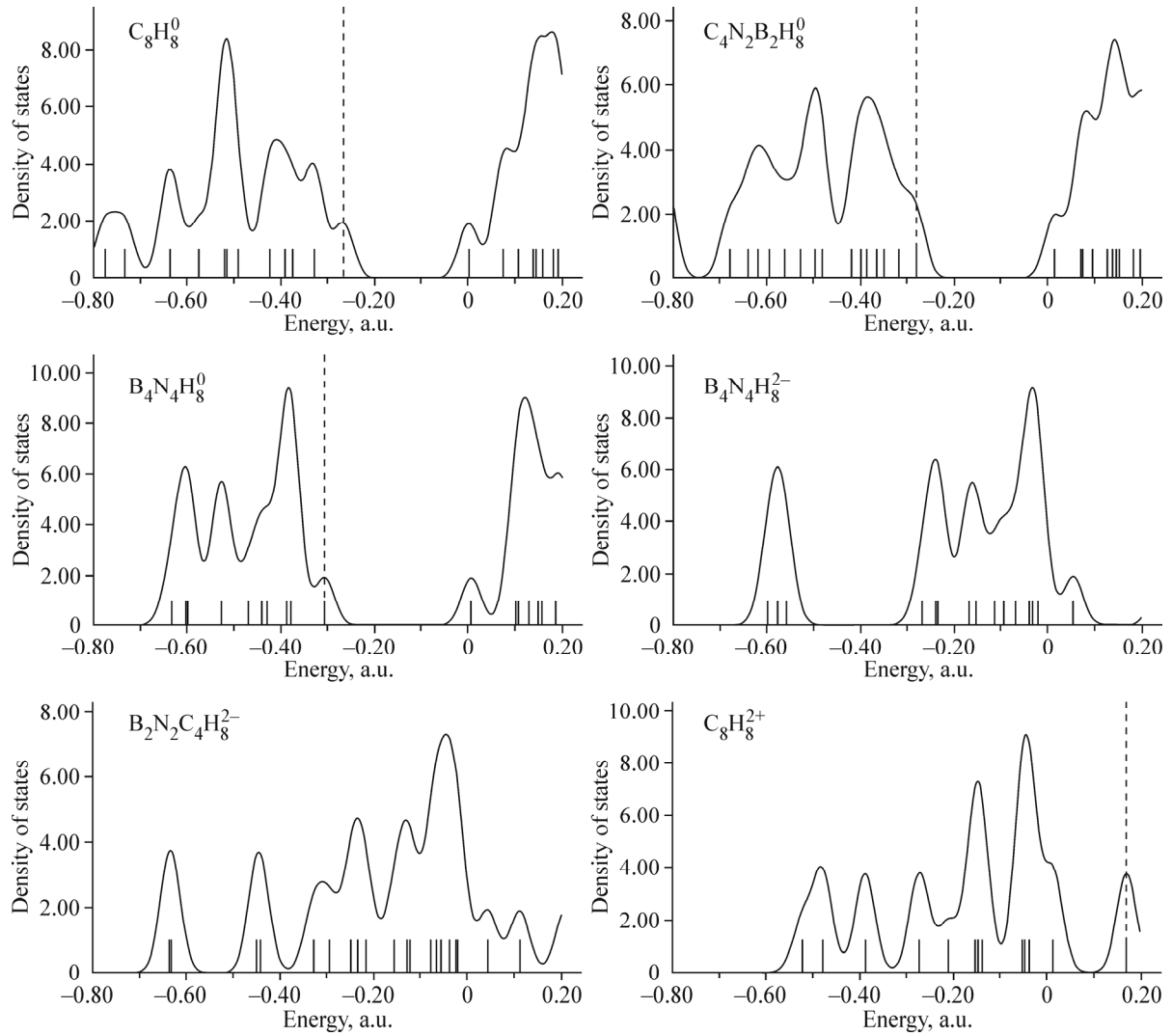

Fig. 4. Total density of states of the molecules and ions.

the electron transport in molecular junctions it is useful to introduce the coupling strength (Γ). For instance, the density of states for benzene (an aromatic molecule) is weakly coupled to featureless leads (Γ = 0.05). As can be seen in Fig. 4, Γ sequences for these molecules are approximately equal, while for $C_4B_2N_2H_8$ they are smaller than for the others.

The maps obtained by the NBO and Multiwfn software indicate total *p* and *s* contributions for induced current densities of each molecule. As expected, the currents from *p* electrons are strongly diatropic in benzene and strongly paratropic in COT (Figs. 3-5). The currents are overmatched by HOMO contributions in both cases. The angular momentum analysis exhibits how the symmetry rules account for these aspects. At each consecutive energy level, the quantum number ($l = 0, 1, \ldots, N/2$) increases by one. In a cycle with $N = 4n+2$ electrons, the HOMO and LUMO correspond to $n = \alpha$ and $n = \alpha + 1$, respectively. It is notable that photo-excited COT relaxes toward the planar D_{8h} symmetry and its structure appears to be identical to the thermal double bond shift transition state. This is a typical π-delocalized structure expected to characterize a Hückel anti-aromatic [4*n*] system. As can be seen from Tables 3 and 4 (% atomic composition of HOMO, LUMO, and HOMO–1), in the aza-bora-heterocycles, some electrons are localized and some others are not. For benzene, low energies may involve only one delocalized allyl radical and three adjacent unpaired electrons, while in COT, due to its larger size, a new and more stable tetraradical configuration might be possible.

Total densities of states of these molecules and ions are plotted in Figs. 3 and 4. As can be seen, for all systems the energies are distributed between –0.8 a.u. and 0.2 a.u. For $B_4N_4H_8^0$, $C_8H_8^0$, $B_2N_2C_4H_8^0$ molecules, which exhibit antiaromaticity, the densities are in the energy ranges from –0.2 to 0.0 while for molecules with the aromaticity behavior they are not zero.

LOLs for variants of $B_4N_4H_8^{2-}$ and $C_8H_8^{2-}$ bonds are plotted in Fig. 5. The locations of sharp peak and distances between two sharp peaks in each bond correspond to σ or π bonds. COTs have extended delocalized structures (i.e., identical to 1.40 Å π bonds and planarity, recalling an aromatic system).

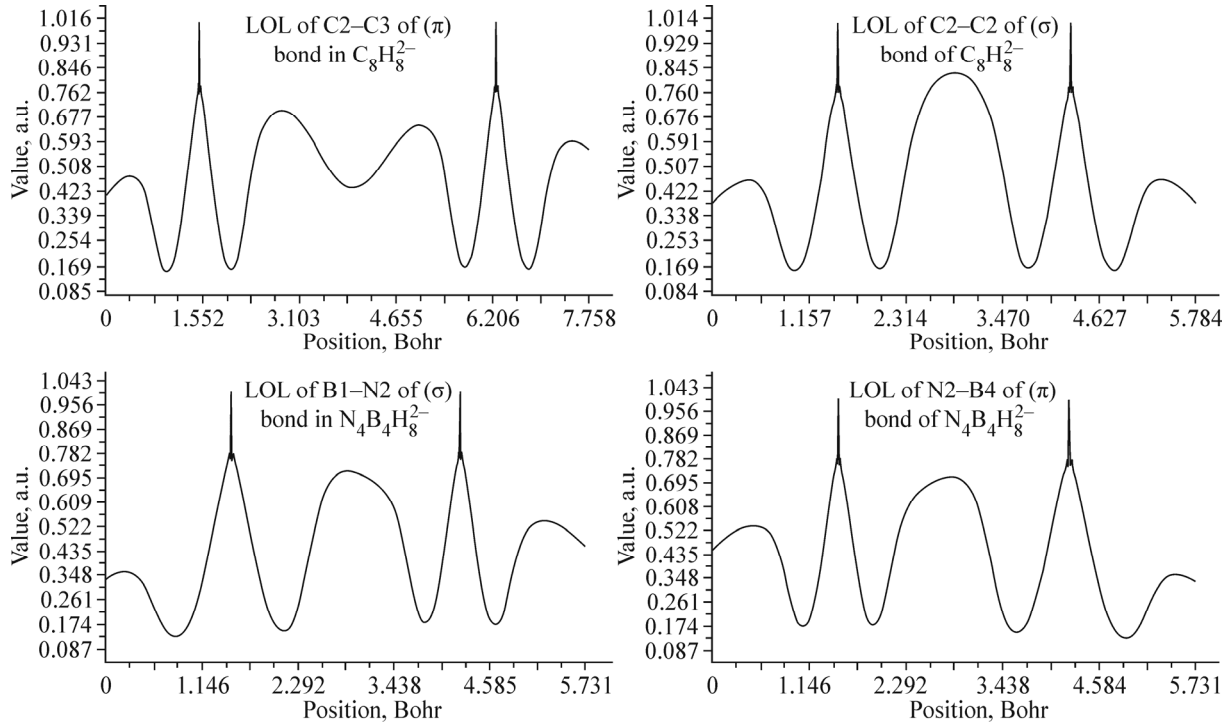

Fig. 5. LOL for $B_4N_4H_8^{2-}$ and $C_8H_8^{2-}$ bonds.

Therefore, it can be suggested that **COT** being stabilized by aromatic effects, which act against the out-of-plane deformation, are needed to reach both *boat* and kink structures due to the motions that break delocalization. The charge and bond order calculations for several variants of $C_8H_8^{n+2}$ (n = –6, –4, –2, 0) are listed in Table 8 and plotted in Fig. 5. Since the bond orders are integer numbers of chemical bonds in molecules which have resonance or non-classical bonding, the bond order may be not integer. In other words, delocalized molecular orbitals contain π orbitals, essentially yielding half π together with σ https://en.wikipedia.org/wiki/Sigma_bond bonds for each pair of atoms. But generally, a calculated bond order being not 1.5 depends on complex scenarios and essentially refers to the bond strength relative to bonds with order 1. Based on our calculation summarized in in Table 8, the Wiberg and fuzzy bond order methods correspond to the molecules with anti-aromatic and aromatic properties, respectively. Since the magnitude of the bond order is associated with the bond length, LOL bonds were calculated and estimated for any further analysis (Fig. 5).

TABLE 8. Various Charge and Bond Order Calculations for $C_8H_8^{2-}$ and $C_8H_8^{2+}$

Molecule		Mayer valence	Wiberg bond order	Mülliken bond order	Fuzzy bond order	Laplacian bond order
$B_4N_4H_8^0$	N1, H9	3.65, 0.98	N1–B2:1.34	N1–B2:1.06	N1–B2:1.28	N1–B2:0.79
	B2, H10	3.85, 0.92	N1–B2:1.34	N1–B2:1.06	N1–B2:1.28	N1–B2:0.79
	B3, H11	3.85, 0.92	B2–N4:1.34	B2–N4:1.06	B2–N4:1.28	B2–N4:0.79
	N4, H12	3.65, 0.98	B3–N6:1.34	B3–N6:1.06	B3–N6:1.28	B3–N6:0.79
	B5, H13	3.85, 0.92	N4–B5:1.34	N4–B5:1.06	N4–B5:1.28	N4–B5:0.79
	N6, H14	3.65, 0.98	B5–N7:1.34	B5–N7:1.06	B5–N7:1.28	B5–N7:0.79
	N7, H15	3.65, 0.98	N6–B8:1.34	N6–B8:1.06	N6–B8:1.28	N6–B8:0.79
	B8, H16	3.85, 0.92	N7–B8:1.34	N7–B8:1.06	N7–B8:1.28	N7–B8:0.79
$C_8H_8^{2-}$	C1, H9	3.83, 0.93	C1–C2: 1.395	C1–C2: 1.00	C1–C2: 1.475	C1–C2: 1.03
	C2, H10	3.83, 0.93	C2–C3: 1.395	C2–C3: 1.00	C2–C3: 1.475	C2–C3: 1.03
	C3, H11	3.83, 0.93	C3–C4: 1.395	C3–C4: 1.00	C3–C4: 1.475	C3–C4: 1.03
	C4, H12	3.83, 0.93	C4–C5: 1.395	C4–C5: 1.00	C4–C5: 1.475	C4–C5: 1.03
	C5, H13	3.83, 0.93	C5–C6: 1.395	C5–C6: 1.00	C5–C6: 1.475	C5–C6: 1.03
	C6, H14	3.83, 0.93	C6–C7: 1.395	C6–C7: 1.00	C6–C7: 1.475	C6–C7: 1.03
	C7, H15	3.83, 0.93	C7–C8: 1.395	C7–C8: 1.00	C7–C8: 1.475	C7–C8: 1.03
	C8, H16	3.83, 0.93	C8–C1: 1.395	C8–C1: 1.00	C8–C1: 1.475	C8–C1: 1.03
$C_8H_8^{2+}$	C1, H9	3.83, 0.93	C1–C2: 1.395	C1–C2: 1.395	C1–C2: 1.46	C1–C2: 1.04
	C2, H10	3.83, 0.93	C2–C3: 1.395	C2–C3: 1.395	C2–C3: 1.46	C2–C3: 1.04
	C3, H11	3.83, 0.93	C3–C4: 1.395	C3–C4: 1.395	C3–C4: 1.46	C3–C4: 1.04
	C4, H12	3.83, 0.93	C4–C5: 1.395	C4–C5: 1.395	C4–C5: 1.46	C4–C5: 1.04
	C5, H13	3.83, 0.93	C5–C6: 1.395	C5–C6: 1.395	C5–C6: 1.46	C5–C6: 1.04
	C6, H14	3.83, 0.93	C6–C7: 1.395	C6–C7: 1.395	C6–C7: 1.46	C6–C7: 1.04
	C7, H15	3.83, 0.93	C7–C8: 1.395	C7–C8: 1.395	C7–C8: 1.46	C7–C8: 1.04
	C8, H16	3.83, 0.93	C8–C1: 1.395	C8–C1: 1.395	C8–C1: 1.46	C8–C1: 1.04
$B_4N_4H_8^{2-}$	B1, H9	3.35, 0.86	B1–N2: 1.244	B1–N2: 0.78	B1–N2: 1.30	B1–N2: 0.44
	N2, H10	2.98, 0.90	B1–N3: 1.244	B1–N3: 0.78	B1–N3: 1.30	B1–N3: 0.45
	N3, H11	2.98, 0.90	N2–B4: 1.244	N2–B4: 0.78	N2–B4: 1.30	N2–B4: 0.45
	B4, H12	3.35, 0.86	B4–N5: 1.244	B4–N5: 0.78	B4–N5: 1.30	B4–N5: 0.44
	N5, H13	2.98, 0.90	N5–B7: 1.244	N5–B7: 0.78	N5–B7: 1.30	N5–B7: 0.45
	B6, H14	3.35, 0.86	B7–N8: 1.244	B7–N8: 0.78	B7–N8: 1.30	B7–N8: 0.44
	B7, H15	3.35, 0.86	N8–B6: 1.244	N8–B6: 0.78	N8–B6: 1.30	N8–B6: 0.44
	N8, H16	2.98, 0.90	B6–N3: 1.244	B6–N3: 0.78	B6–N3: 1.30	B6–N3: 0.44

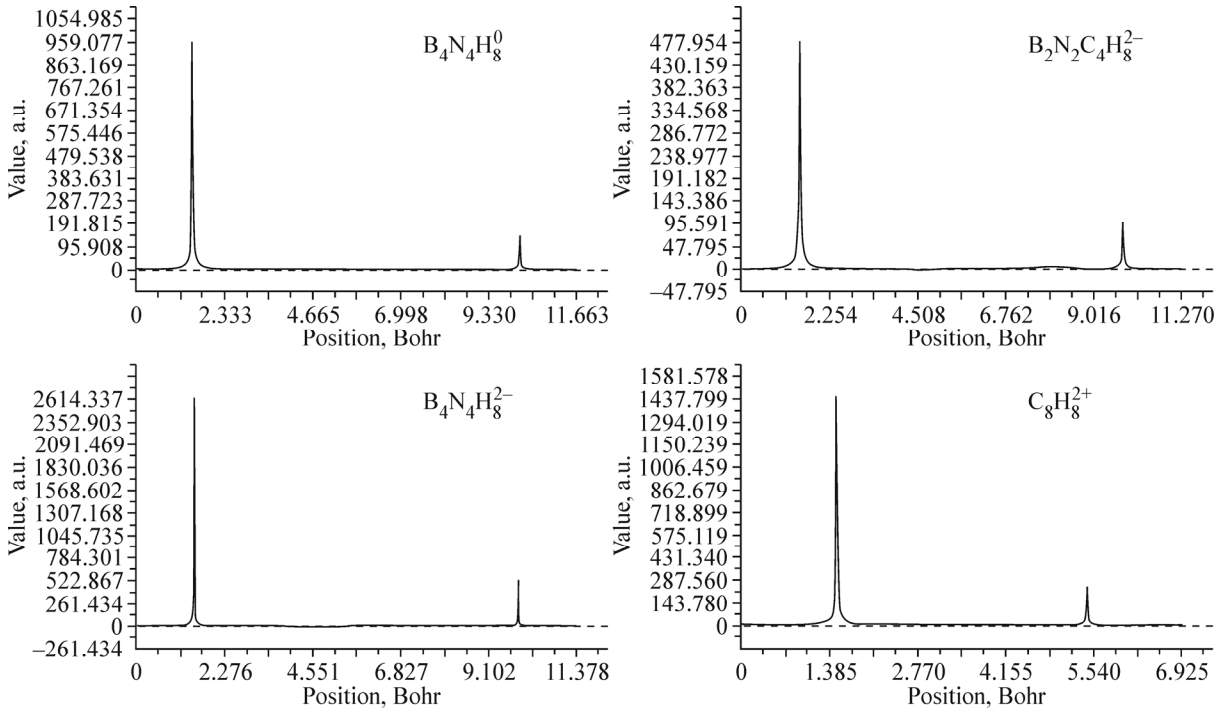

Fig. 6. Total electrostatic potentials for $B_4N_4H_8^0$, $B_2N_2C_4H_8^{2-}$, $B_4N_4H_8^{4-}$, and $C_8H_8^{2+}$.

As can be seen in Fig. 6, the variants start to be electrostatically stable around the bond length positions. Total electrostatic potentials for $B_4N_4H_8^0$, $B_2N_2C_4H_8^{2-}$, $B_4N_4H_8^{4-}$, and $C_8H_8^{2+}$ are shown in Fig. 6 where sharp peaks are located at 1.166, 1.127, 1.138, and 1.385, respectively.

CONCLUSIONS

Current density maps, ELF, and LOL from ab initio calculations of $C_8H_8^{n+2}$ (n = –4, –2, 0) and $B_n N_nC_{(8-2n)}H_8$ (n = 2, 4) are investigated as a novel method for understanding aromaticity and antiaromaticity in heterocyclic compounds. For each molecule, the maps indicate total ρ and s contributions for inducing the current density. As expected, the currents arising from p electrons are strongly diatropic in benzene and strongly paratropic in COT. The angular momentum analysis shows how the symmetry rules account for these aspects. The currents are dominated by HOMO contributions in both cases. The HOMO/LUMO overlap in whole spaces indicates the sum over states, producing a strong two-electron paramagnetic ring current. Other rotational and translational transitions presented through the symmetry lowering actually have a minor importance in small cycles. Antiaromaticity is a result of the HOMO/HOMO–1 overlap in whole spaces.

ACKNOWLEDGMENTS

The common idea and preliminary discussion of this work refer to the duration of my sabbatical collaboration with Prof. James E. Boggs (who passed away) in the Institute for Theoretical Chemistry, Department of Chemistry and Biochemistry, The University of Texas at Austin, Austin, Texas, United States and is devoted to his memory.

CONFLICT OF INTERESTS

The author declares that he has no conflict of interests.

REFERENCES

1. P. G. Wenthold, D. A. Hrovat, and W. T. Borden. *Science*, **1996**, *272*, 1456–1459.
2. T. Nishinaga, T. Ohmae, and M. Iyoda. *Symmetry*, **2010**, *2*, 76–97.
3. R. Naor and Z. Luz. *J. Chem. Phys*., **1982**, 76, 5662–5664.
4. T. A. Keith and R. F. W. Bader. *Chem. Phys. Lett*., **1992**, *194*(1), 1–8, DOI: 10.1016/0009-2614(92)85733-Q.
5. J. L. Andrés, O. Castaño, A. Morreale, R. Palmeiro, and R. Gomperts. *J. Chem. Phys*., **1998**, *108*, 203–207.
6. C. Tokizaki, T. Yoshida, and T.Takayanagi. *Comput. Theor. Chem.*, **2017**, *1112*, 20–26.
7. R. Willstätter and E. Waser. *Ber. Dtsch. Chem. Ges.*, **1911**, *44*(3), 3423–3445.
8. O. Schlichting, K. Klager, and T. Toepel. *Liebigs Ann. Chem.*, **1948**, *560*(1), 1–92.
9. W. J. I. Fernández, Y. Mo, and P. v. R. Schleyer. *J. Chem. Theor. Comput*., **2012**, *8*, 1280–1287.
10. D. A. Hrovat and W. T. Borden. *J. Am. Chem. Soc.*, **1992**, *114*, 5879–5881.
11. C. Gellini and P. R. Salvi. *Symmetry*, **2010**, *2*, 1846–1924.
12. A. Schild and B. Paulus. *J. Comput. Chem.*, 2013, *34*, 1393–1397.
13. C. D. Stevenson, E. C. Brown, D. A. Hrovat, and W. T. Borden. *J. Am. Chem. Soc*., **1998**, *120*, 8864–8867.
14. Z. Badri and C. Foroutan-Nejad. *Phys. Chem. Chem. Phys.*, **2016**, *18*(17), 11693–11699, DOI: 10.1039/c5cp05222j.
15. T. A. Keith and R. F. W. Bader. *Chem. Phys. Lett*., **1993**, *210*(1), 223–231, DOI: 10.1016/0009-2614(93)89127-4.
16. T. A. Keith and R. F. W. Bader. *J. Chem. Phys*., **1993**, *99*(5), 3669–3682, DOI: 10.1063/1.466165.
17. T. A. Keith. *Chem. Phys*., **1996**, *213*(1), 123–132, DOI: 10.1016/S0301-0104(96)00272-8.
18. T. A. Keith and R. F. W. Bader. *Can. J. Chem*., **1996**, *74*(2), 185–200, DOI: 10.1139/v96-022.
19. F. London. *J. Phys. Radium*, **1937**, *8*, 397–409.
20. L. Pauling. *J. Chem. Phys*., **1936**, *4*, 673–677.
21. J. A. Pople. *J. Chem. Phys*., **1956**, *24*, 1111.
22. P. v. R. Schleyer, C. Maerker, A. Dransfeld, H. Jiao, and N. J. R. E. Hommes. *J. Am. Chem. Soc*., **1996**, *118*, 6317–6318.
23. A. Soncini, P. W. Fowler, and L. W. Jenneskens. *Phys. Chem. Chem. Phys*., 2004, *6*, 277–284.
24. F. A. L. Anet and D. J. O′Leary. *Concepts Magn. Reson*., **1992**, *4*, 35.
25. U. Haeberlen. High Resolution NMR in Solids: Selective Averaging. Advances in Magnetic Resonance Supplement 1. Academic Press: New York, **1976**.
26. M. Mehring. Principles of High Resolution NMR in Solids. Springer: Berlin, **1983**.
27. NMR Basic Principles and Progress / Eds. P. Diehl, E. Fluck, H. Günther, R. Kosfeld, and J. Seelig. Vol. 15. Springer: Berlin, **1978**.
28. J. Herzfeld and A. E. Berger. *J. Chem. Phys*., **1980**, *73*, 6021.
29. R. F. W. Bader. Atoms in Molecule: A Quantum Theory. Oxford Univ. Press: Oxford, **1990**.
30. A. D. Becke and K. E. Edgecombe. *J. Chem. Phys.*, **1990**, *92*, 5397.
31. A. Savin, O. Jepsen, J. Flad, O. K. Andersen, H. Preuss, and H. G. V. Schnering. *Angew. Chem.*, *Int. Ed. Engl*., **1992**, *31*, 187.
32. A. D. Becke. *J. Mol. Struct*.: *THEOCHEM*, **2000**, *527*, 51–56.
33. W. Kohn and L. J. Sham. *Phys. Rev. A*, **1965**, *140*, 1133–1138.
34. T. Lu and F. Chen. *J. Mol. Graphics Modell.*, **2012**, *38*, 314–323.
35. T. Lu and F. A. Chen. *J. Comput. Chem*., **2012**, *33*, 580–592.
36. B. H. Besler, K. M. Merz, and P. A. Kollman. *J. Comput. Chem*., **1990**, *11*, 431–439.
37. L. E. Chirlian and M. M. Francl. *J. Comput. Chem*., **1987**, *8*, 894–905.
38. F. Martin and H. Zipse. *J. Comput. Chem*., **2005**, *26*, 97–105.
39. M. Monajjemi, V.S. Lee, M. Khaleghian, B. Honarparvar, and F. Mollaamin. *J. Phys. Chem. C*, **2010**, *114*, 15315.

40. M. Monajjemi and M. Khaleghian. *J. Clust. Sci.*, **2011**, *22*, 673–692.
41. M. Monajjemi. *Struct. Chem.*, **2012**, *23*, 551.
42. M. Monajjemi and J. E. Boggs. *J. Phys. Chem. A*, **2013**, *117*, 1670–1684.
43. M. Monajjemi, W. J. Robert and J. E. Boggs. *Chem. Phys.*, **2014**, *433*, 1–11.
44. F. Mollaamin, T. T. Pham, D. M. T. Dang, M. Monajjemi, and C. M. Dang. *Biointerface Res. Appl. Chem.*, **2019**, *9*(4), 4050–4059.
45. M. Monajjemi. *Theor. Chem. Acc.*, **2015**, *134*, 1668–1669.
46. M. Monajjemi. *J. Mol. Model.*, **2014**, *20*, 2507.
47. M. Monajjemi and N. T. Mohammadian. *J. Comput. Theor. Nanosci.*, **2015**, *12*, 4895–4914.
48. A. A. Frost and B. Musulin. *J. Chem. Phys.*, **1953**, *21*, 572.
49. A. Matsuura and K. Komatsu. *J. Am. Chem. Soc.*, **2001**, *123*, 1768–1769.
50. A. J. Bridgeman. *Polyhedron*, **1998**, *17*, 2279–2288.
51. E. W. Stout and P. Politzer. *Theor. Chim. Acta*, **1968**, *12*(5), 379–386.